

Ab initio study on the magneto-structural properties of MnAs

Ivan Rungger and Stefano Sanvito
School of Physics, Trinity College, Dublin 2, Ireland
(Dated: June 27, 2018)

The magnetic and structural properties of MnAs are studied with *ab initio* methods, and by mapping total energies onto a Heisenberg model. The stability of the different phases is found to depend mainly on the volume and on the amount of magnetic order, confirming previous experimental findings and phenomenological models. It is generally found that for large lattice constants the ferromagnetic state is favored, whereas for small lattice constants different antiferromagnetic states can be stabilized. In the ferromagnetic state the structure with minimal energy is always hexagonal, whereas it becomes orthorhombically distorted if there is an antiferromagnetic component in the hexagonal plane. For the paramagnetic state the stable cell is found to be orthorhombic up to a critical lattice constant of about 3.7 Å, above which it remains hexagonal. This leads to the second order structural phase transition between paramagnetic states at about 400 K, where the lattice parameter increases above this critical value with rising temperature due to the thermal expansion. For the paramagnetic state an analytic approximation for the magnitude of the orthorhombic distortion as a function of the lattice constant is given. Within the mean field approximation the dependence of the Curie temperature on the volume and on the orthorhombic distortion is calculated. For orthorhombically distorted cells the Curie temperature is much smaller than for hexagonal cells. This is mainly due to the fact that some of the exchange coupling constants in the hexagonal plane become negative for distorted cells. This is also the reason for the appearance of canted spin structures at low temperatures and high pressures, where the cell is orthorhombic. With these results a description of the susceptibility as function of temperature is given, where the temperature dependence enters via the dependence of the Curie temperature on the lattice parameters.

I. INTRODUCTION

MnAs is an extremely promising material for magneto-electronics, since it can grow epitaxially on GaAs¹ and Si² forming clean and atomically sharp interfaces.² MnAs/GaAs heterojunctions have been extensively studied experimentally,^{1,3,4,5} and spin injection from MnAs into GaAs has been demonstrated.⁶ However one of the major drawbacks for the use of MnAs in devices is the fact that bulk MnAs has a phase transition at 318 K, where the magnetic state changes from ferromagnetic to paramagnetic. Moreover when grown on GaAs, this temperature changes depending on the growth direction. This is mainly attributed to the induced strain.^{1,3,7,8} The aim of this paper is to use *ab initio* density functional theory (DFT) calculations to develop a theory of the phase transitions of MnAs, which can be compared with experiments and with existing phenomenological models.

First a review of the experimental properties of MnAs is presented, and a brief description of the existing phenomenological models is given. Then the results of our *ab initio* calculations are presented and compared to experiments and phenomenological models. Within the scope of a Heisenberg model the exchange coupling constants are calculated for different distorted unit cells, and the Curie temperature and its dependence on the lattice parameters are evaluated in the mean field approximation. The use of the Heisenberg model also makes possible the prediction of the ground state volume and lattice structure for the paramagnetic state. It will be shown that the phase transitions of MnAs can indeed be explained by *ab initio* calculations. In the last section our results are summarized and a simple model for the susceptibility

as function of temperature is given. From these a semi-quantitative description of the phase diagram of MnAs will emerge.

II. EXPERIMENTAL PROPERTIES AND EXISTING MODELS

A. Experimental properties

MnAs is a ferromagnetic metal at low temperature, but it becomes paramagnetic at $T_p = 318$ K. At this critical temperature the magnetic moment changes abruptly from a finite value to zero (figure 1), the resistivity increases discontinuously,⁹ the volume is reduced by 2.1%, and the lattice structure changes from the hexagonal B8₁ (NiAs-type) to the orthorhombic B31 (MnP-type) structure.^{10,11,12,13,14} The B31 structure is obtained by slightly distorting the B8₁ structure. Associated with this transition there is a latent heat of 7490 J/kg.¹¹ Furthermore the phase transition shows hysteresis with a critical temperature of 307 K upon cooling and of 318 K upon heating.¹³ All these properties clearly indicate that the phase transition is of first order.

Above T_p the distortion of the crystal structure reduces continuously, until it vanishes at $T_t \approx 398$ K.¹⁰ At T_t MnAs undergoes another phase transition, where it changes back from the B31 structure to the B8₁ structure. The lattice dimensions change continuously and there is no latent heat, but only a discontinuity in the heat capacity of the material. Therefore this phase transition is of second order. For temperatures between T_p and T_t the paramagnetic susceptibility of the material

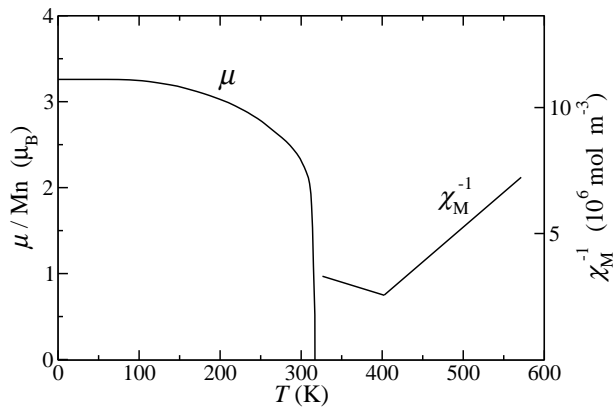


FIG. 1: Magnetization per Mn atom μ as a function of temperature for ferromagnetic MnAs below 318 K, and inverse susceptibility χ_M^{-1} for paramagnetic MnAs above 318 K (schematically after reference [14]).

has an anomalous behavior. It increases with increasing temperature until it reaches a maximum at T_t . Above T_t it decreases and has a Curie-Weiss behavior (figure 1). Moreover at T_t there is a lambda point in the specific heat.¹⁵ Application of a magnetic field is found to transform the B31 structure back to the B8₁ above a critical field.^{9,16,17,18,19} Table I gives a short summary of the described properties of MnAs.

Figure 2 shows the phase diagram of MnAs. If pressure is applied to the system, T_p is lowered, while T_t increases. Above a critical pressure of 4.6 kbar the ferromagnetic B8₁ structure becomes unstable, and the material has the B31 structure for all temperatures below T_t . At high pressures and low temperatures different types of ordered magnetic structures are found, with a reduced saturation magnetic moment with respect to the zero pressure ferromagnetic phase. This, together with the anomalous behavior of the susceptibility between T_p and T_t , led Goodenough to the idea that the magnetic moment of the Mn atoms changes from a high spin state in the B8₁ structure to a low spin state in the B31 structure.^{13,14} According to his idea in the B31 structure the moment of the Mn atoms lies between 1 and 2 μ_B . However neutron scattering experiments on MnAs samples in the B31 structure have shown that the local magnetic moment of the Mn atoms lies between 3 and 3.4 μ_B for different temperatures and pressures,²⁰ in clear contradiction to the assumption of a low spin state. Canted spin structures, similar to the helimagnetic structures of MnP,²¹ are found at a pressure of 4.75 kbar below 210 K, with a local magnetic moment of about 3 μ_B . The different saturation magnetic moments for different pressures therefore correspond to different types of canted magnetic alignments. A hysteresis region lies between the ferromagnetic and the canted regions, where both the B8₁ and the B31 structures can be stabilized.

When the magnetic order breaks down and the system becomes paramagnetic, it has the B31 structure for all

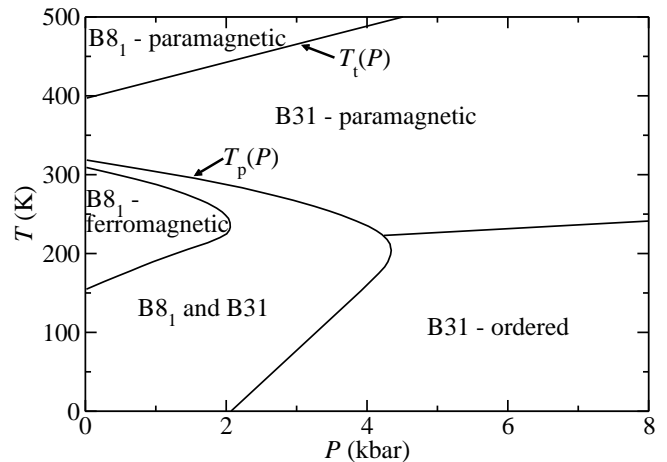


FIG. 2: Temperature (T) versus pressure (P) phase diagram of MnAs (adapted from reference [14]), indicating also T_p and T_t as functions of pressure.

pressures. As the temperature is further increased the structure of the cell continuously changes back towards the B8₁, until at T_t it has again the B8₁ structure, with $\partial T_t / \partial P > 0$, where P is the pressure.

The magnetocrystalline anisotropy is quite strong in MnAs, with the c -axis being the hard axis, so that the moments prefer to lie in the hexagonal plane.¹² Measurements on the magnetoelastic coupling²² indicate that the coupling is stronger in the hexagonal plane than perpendicular to it.

Figure 3 shows the unit cells of MnAs in the hexagonal B8₁ and in the orthorhombic B31 crystal structures and it defines the unit cell vectors \mathbf{a} , \mathbf{b} (\mathbf{b}_h for the B8₁ structure) and \mathbf{c} . The B8₁ structure consists of stacked hexagonal layers of Mn and As atoms, and the unit cell contains two Mn and two As atoms. The B31 structure has twice the volume of the B8₁ due to symmetry lowering and contains four Mn and four As atoms. The lattice is nearly hexagonal, and the atoms are moved out of the hexagonal symmetry points along the \mathbf{b} and \mathbf{c} directions (figure 3(b)).

The Mn atoms are mainly displaced in the hexagonal plane along the \mathbf{b} direction, to form chains of closer Mn atoms, separated from the other chains by a larger distance (figure 4). The As atoms are mainly displaced along the \mathbf{c} axis. In each unit cell one of the planar As atoms is moved upwards and the other downwards with respect to the original position in the B8₁ structure, so as to keep the Mn-As distance nearly constant. The displacement u of the Mn atoms in the hexagonal plane lies between 0 and 0.05 b ($b = |\mathbf{b}|$), depending on the temperature and pressure, and the displacement v of the As atoms along the c -axis lies between 0 and 0.05 c ($c = |\mathbf{c}|$). The B8₁ structure is a special case of the B31 structure, where $b = \sqrt{3} a$ and $u = v = 0$.

Therefore we choose the unit cell vectors in such a way that \mathbf{a} and \mathbf{c} have the same direction for both the B8₁

| | $0 < T < T_p$ | $T_p < T < T_t$ | $T_t < T$ |
|-----------------------|---------------------------|-------------------------------|-------------------------------|
| Crystal structure | Hexagonal B8 ₁ | Orthorhombic B31 | Hexagonal B8 ₁ |
| Magnetic order | Ferromagnetic | Paramagnetic | Paramagnetic |
| Magnetic moment | $3.4\mu_B$ | -- | -- |
| Susceptibility χ | -- | $\partial\chi/\partial T > 0$ | $\partial\chi/\partial T < 0$ |

TABLE I: Some properties of MnAs at zero pressure.¹³

and the B31 structures. In contrast the directions of the vectors \mathbf{b}_h ($|\mathbf{b}_h| = |\mathbf{a}| = a$) for the hexagonal cell and \mathbf{b} for the orthorhombic cell are different.

The lattice parameters of MnAs as function of temperature and magnetic field have been measured in several works [10,18,23,24]. Figure 5 shows the change of the lattice parameters as a function of temperature for zero pressure.¹⁰ The lattice parameters increase with temperature due to normal thermal expansion. However the in plane lattice parameter a decreases when the temperatures get near T_p , where it jumps from 3.717 Å to the lower value of 3.673 Å. The perpendicular lattice parameter c always increases continuously with temperature. At T_t there is an inflection in the slope of the lattice parameter as a function of temperature, and at about $T_s = 450$ K the slope changes discontinuously. In other measurements the discontinuous change of the slope is found at about 410 K.²⁴

The exact temperature at which the distortion disappears is somewhat uncertain, and fluctuations may play a role for small distortions. The given temperature for the disappearing of the distortion correspond to $T_t = 398$ K,^{10,24} however measurements for small distortions are difficult and such temperature can only be inferred. As pointed out in reference [25] the distortion should appear at temperatures slightly above T_t . Throughout this work we assume that the disappearing of the distortion occurs at T_s , which is the temperature where the thermal expansion coefficient of MnAs changes abruptly.

B. Review of existing models

Until the fifties it was believed that the first order phase transition at T_p was between a ferromagnetic and an antiferromagnetic state. Kittel then proposed a model where the distortion from the B8₁ to the B31 structure produces the change in sign of one of the exchange coupling constants, giving rise to antiferromagnetic order.²⁶ However there was no experimental evidence of this antiferromagnetic state and experiments demonstrated that the transition is instead to a paramagnetic state.²⁴

Therefore Bean and Rodbell (BR) proposed a modification of Kittel's theory, where the exchange interactions are ferromagnetic for both structures, but they are much weaker in the B31 phase.^{11,27} The main idea is that

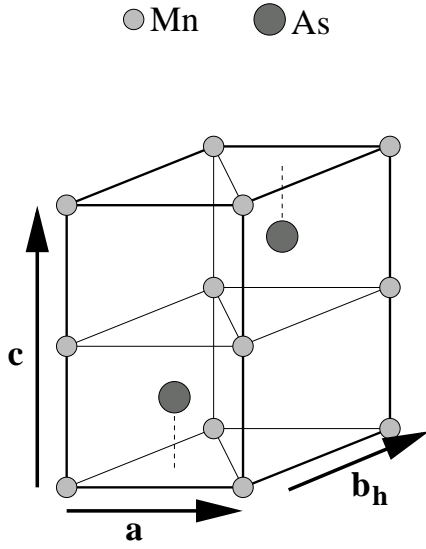
the exchange interaction decays strongly as the volume decreases. In order to simplify the model, the analysis was based on the extrapolated Curie temperature T_C only, and not on the details of the magnetic interaction at the atomic level. Furthermore the model neglected the anisotropic change of the crystal structure, and assumed that it is possible to describe the change from the B8₁ to the B31 structure by a change in volume only. The dependence of T_C on the volume V was described by the following equation

$$T_C = T_0 \left[1 + \beta \frac{(V - V_0)}{V_0} \right], \quad (1)$$

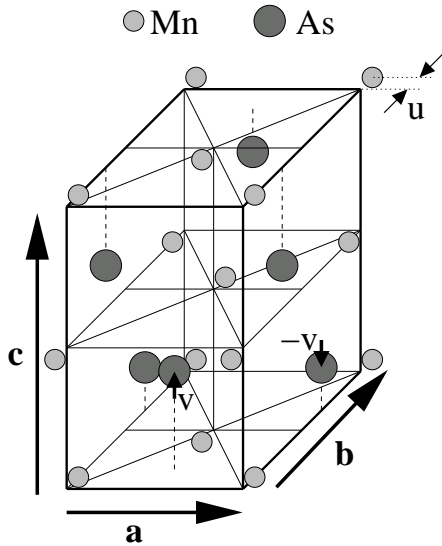
where T_0 is the Curie temperature at the volume V_0 , which is the volume that the system would have in the hypothetical absence of exchange interaction. In this context this corresponds to the volume of the B31 structure above T_p . β is a parameter and is determined by fitting the model to experiments. Within the BR model one can show that for certain values of β a first order phase transition between a ferromagnetic and paramagnetic state occurs with a simultaneous change of the volume. However the model does not explain the second order phase transition at T_t . Further improvements such as the introduction of a term proportional to $(V - V_0)^2$ do not change the main results.²⁸

Later Goodenough made an attempt to explain the anomalous behavior of the susceptibility and the second order phase transition at T_t by extending the BR model and assuming that the local magnetic moment on the Mn atoms depends strongly on the volume.^{13,14} Here the Mn atoms are assumed to be in a high spin state in the B8₁ structure and in a low spin state in the B31 structure.^{13,14} However measurements of the local magnetic moment show that the change in the magnetic moment at T_p is very small, therefore the Goodenough model is not applicable to this phase transition. This is probably due to the fact that the MnAs unit cell volume in any crystalline structure is too big to justify a high-spin to low-spin transition. In fact in $\text{MnAs}_{1-x}\text{P}_x$ the change from high-spin to low-spin state is observed,^{10,29,30} however the low spin state is found for unit cell volumes smaller than 120 Å³. In contrast the unit cell of MnAs has always a volume of around 130 Å³, and it is always in the high-spin state.

In 1982 Kato et al. extended the BR model by taking into account not only the change in volume, but also



(a)



(b)

FIG. 3: (a) B8₁ unit cell containing two Mn and two As atoms, (b) B31 unit cell containing four Mn and four As atoms.

the change of the crystal structure.³¹ Furthermore instead of just using T_C for describing the magnitude of the exchange interactions, they consider exchange coupling constants up to second nearest neighbors. The obtained results are similar to those of Bean and Rodbell. The second order phase transition at T_t is explained by assuming that locally the structure above T_t is still the B31, but that the distortions from the B8₁ are randomly distributed. This assumption is probably not valid, since

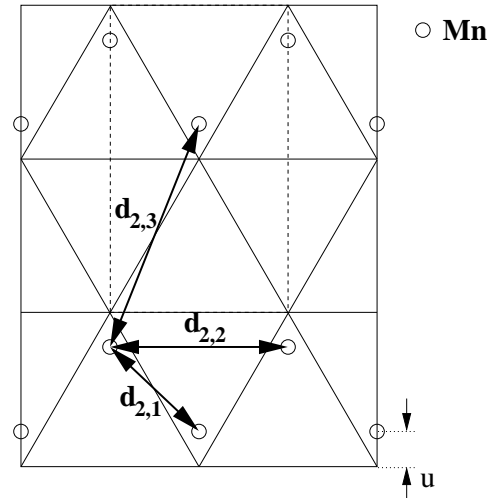


FIG. 4: Two-dimensional representation of one layer of Mn atoms in the B31 structure. d_{ij} represent the various Mn-Mn distances. The first index $i=2$ indicates that all the Mn are second nearest-neighbor to each other in the B8₁ structure. The second index $j=1, 2, 3$ labels the three distances arising from the B31 distortion.

neutron diffraction experiments clearly indicate that the structure is a regular B8₁ above T_t .²⁴

A Landau-type phenomenological model, where the free energy Φ is expanded as a function of order parameters, is given in references [25,32,33] and references therein. In reference [25] just two order parameters are used, the relative magnetization σ ($\sigma = 1$ for a ferromagnetic state, $\sigma = 0$ for a paramagnetic state) and the orthorhombic distortion d . The following equation is used for the free energy:

$$\Phi(d, \sigma; T, H) = \Phi_0 + c_1 (T - T_0 (1 - \delta_1 d^2)) \sigma^2 + c_2 \sigma^4 + c_3 \sigma^6 + c_4 (T - T_D) d^2 + c_5 d^4 - M_0 \sigma H (1 - \delta_2 d^2), \quad (2)$$

where c_1, \dots, c_5 and δ_1, δ_2 are expansion coefficients to be fitted to experiment, H is an external magnetic field, M_0 is the saturation magnetization, T_0 is the extrapolated Curie temperature of the low temperature phase, and Φ_0 is a constant.

The distortion d plays the same role as the relative change in volume $(V - V_0)/V_0$ of the BR model (equation (1)). In equation (1) T_C depends linearly on the change in volume, whereas now it depends quadratically on the distortion d , $T_C = T_0(1 - \delta_1 d^2)$. This is the correct expansion of T_C , since the linear term in d disappears due to symmetry ($+d$ and $-d$ correspond to the same distortion). The terms in σ^2 , σ^4 and σ^6 appear also in the BR model and lead to the first order transition at T_p . The second order phase transition at $T_t = T_D$ is generated by the d^2 and d^4 terms in the expansion.

Also the variation of the magnetic moment with the distortion is contained in the model, although the authors find that the coefficient δ_2 is essentially zero. For T_0 the

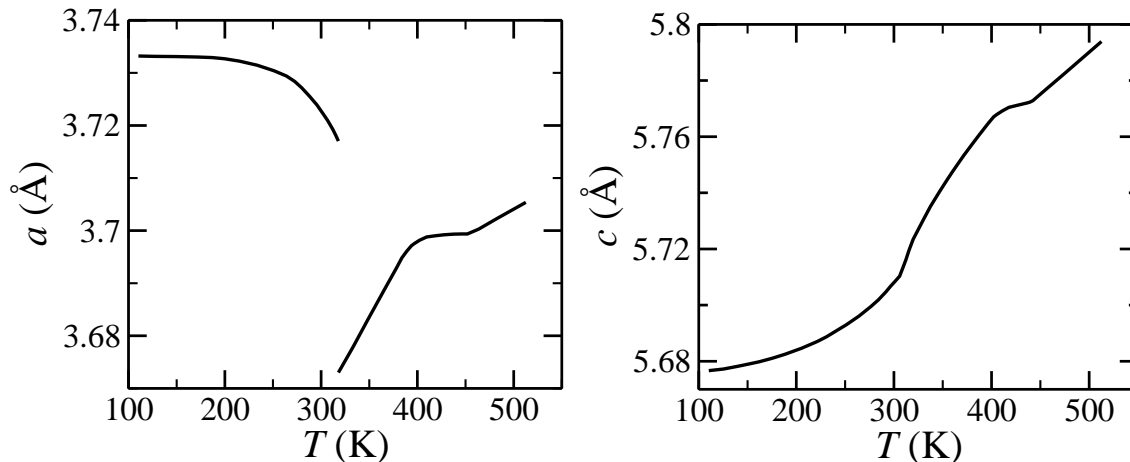


FIG. 5: Lattice parameters a and c (see figure 3) as a function of temperature (after reference [10]).

Curie temperature extrapolated from the high temperature susceptibility above T_t was considered ($T_0 = 285$ K), and for T_D the temperature at which the inverse susceptibility has a minimum ($T_D = 394$ K). By construction this model yields the correct thermodynamic behavior, and also predicts the increase of the susceptibility between T_p and T_t by means of the reduction of the distortion with increasing temperature.

Variations of this model [32,33] give similar results. In reference [33] the full T - P - H phase diagram of MnAs is explained with a Landau-type expansion, where more order parameters are used. However also in this case a term equivalent to $(T - T_D)d^2$ of equation (2) is used in order to obtain the phase transition at T_D . Despite the fact that Landau-type expansions give very good agreement between theory and experiments when the right parameters are used, they do not provide insights into the origin of the terms of the expansion, especially of the $(T - T_D)d^2$ term. In reference [34] a basic justification of such term is given from first principles within a spin fluctuation theory constructed from a Hubbard Hamiltonian. It is shown that for a given volume the minimum of the free energy can lie at $d = 0$ for a ferromagnetic state or at $d \neq 0$ for a paramagnetic state.

In 1986-87 Motizuki and Katoh used spin fluctuation theory in order to explain the anomalous behavior of the susceptibility between T_p and T_t .^{35,36} A Hubbard Hamiltonian was used, with model density of states obtained from first principle calculations. They could qualitatively show that the susceptibility increases when going from the B31 structure to the B8₁ structure, again mainly due to the fact that T_C increases with increasing temperature.

More recently various tight binding^{37,38} as well as first principles^{39,40,41,42,43,44,45,46,47} calculations have been performed for MnAs in the B8₁ structure. The results generally agree and compare well with the experiments. Only two studies on MnAs in the B31 structure are known to the authors.^{48,49} In reference [48] a description of the paramagnetic state of the B31 structure is

given by assuming that the paramagnetic state coincides with zero local magnetic moment of the Mn atoms. This does not correspond to the usual way of describing paramagnetism, which rather corresponds to constant local magnetic moments, whose directions in space change randomly in time due to spin fluctuations.

The present work investigates the magnetic interactions across the various phase transitions of MnAs. An explanation of the magnetostructural properties in terms of first-principles calculations is given, thereby illustrating the origin and providing a justification of the parameters used by the different models.

III. RESULTS

A. DFT calculations

First principles calculations within density functional theory (DFT) are performed using the pseudopotential code based on localized atomic orbitals SIESTA.⁵⁰ The generalized gradient approximation (GGA) is used for the exchange correlation potential,⁵¹ since it has been shown to give good structural properties for hexagonal MnAs.^{39,41,42} In the valence we consider $4s$, $4p$ and $3d$ orbitals for Mn, and $4s$, $4p$ and $4d$ for As. For both Mn and As double zeta polarized local orbitals are used for the s and p angular momenta, whereas for the d orbitals double zeta is used. The number of k -points in the Brillouin zone is specified by a grid cutoff of 20 \AA . This corresponds to a $11 \times 11 \times 8$ mesh for the B8₁ unit cell, giving approximately 1000 k -points in the full Brillouin zone. For the B31 unit cell such cutoff yields a $8 \times 11 \times 7$ mesh. The real space mesh cutoff, which determines the density of the real space grid, is 300 Ry.

After full relaxation of the unit cell to a pressure below 0.1 kbar, and of the atomic positions to a force smaller than 0.01 eV/\AA the B31 unit cell in the ferromagnetic configuration relaxes to a B8₁ structure with $a = 3.72$

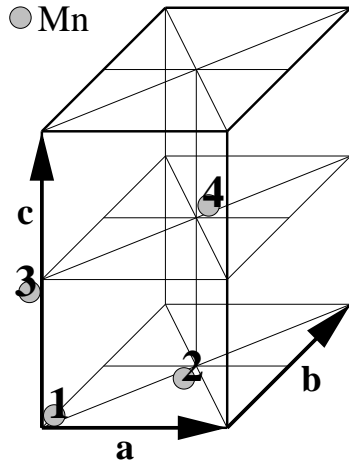


FIG. 6: B31 unit cell where only the four Mn atoms are shown displaced out of the $B8_1$ symmetry positions.

\AA and $c = 5.58 \text{ \AA}$. The experimental values at room temperature are $a = 3.724 \text{ \AA}$ and $c = 5.707 \text{ \AA}$. Therefore the relative error is below 1% for a and -2% for c . The lattice parameters at 110 K can be extracted from figure 5 and are $a = 3.733 \text{ \AA}$ and $c = 5.677 \text{ \AA}$. This demonstrates that GGA-DFT reproduces rather well the zero temperature ground state.

For a fixed c/a ratio of 1.54, which is close to the experimental value at the first order phase transition, the energy is minimized for $a = 3.695 \text{ \AA}$, which compares well with the results of other *ab initio* calculations.^{39,41,42} Also the band structure and the density of states are similar to previous calculations. The magnetic moment per Mn atom is $3.4 \mu_B$, and compares well with the measured value of $3.4 \mu_B$.¹³

The unit cell of the B31 structure contains 4 Mn atoms, allowing for 3 possible independent antiferromagnetic configurations of the local moments of the Mn atoms. The different antiferromagnetic states are $++--$, $+--+$ and $+---$. As a matter of notation $++--$ means that the atoms 1 and 2 in the unit cell have opposite magnetic moment than that of atoms 3 and 4. The indices of the Mn atoms in the unit cell are defined in figure 6. A cell relaxation is performed for those three antiferromagnetic configurations. Table II lists the obtained relaxed structures together with the total energies per Mn atom as compared to the ferromagnetic ground state energy ($E - E_{\text{FM}}$). The structure remains of the $B8_1$ type if the local moments are ferromagnetically aligned in the hexagonal plane, whereas it changes to the B31 type if the moments are antiferromagnetically aligned, with u (v) of the order of $0.05 b$ (c). There is also a slight displacement of the Mn atoms along \mathbf{c} of at most $0.01 c$, and of the As atoms along \mathbf{b} of at most $0.01 b$.

Generally it can be observed that the in-plane lattice parameters contract and the c -parameter expands for the

antiferromagnetic states, resulting in a reduction of the volume V . The calculated values are similar to those given in reference [48].

The total energy for the ferromagnetic alignment is the lowest, although the $+ - - +$ configuration is higher of only 17 meV/Mn . This indicates that the system should evolve to one of the antiferromagnetic states under pressure, since those have a much smaller volume but only a slightly higher energy.

Table II gives also the distances between the first three nearest neighbor Mn atoms in the hexagonal plane $d_{2,1}$, $d_{2,2}$ and $d_{2,3}$ (see figure 4). Note that $d_{2,2} = a$ and it is not given explicitly. While these distances are all equal in the hexagonal case, they differ of as much as 1 \AA in the B31 structure. Large changes in the distance between the Mn atoms are possible since the nearest neighbor Mn-Mn separation in MnAs is well above the inter-atomic distance 2.61 \AA of bulk Mn,⁵² which can be regarded as the minimal possible distance between Mn atoms. The distance between nearest neighbor Mn and As atoms lies between 2.46 \AA and 2.62 \AA for all the different configurations, and changes therefore much less than the Mn-Mn distance.

The local magnetic moment on the Mn (μ_{Mn}) and As (μ_{As}) atoms, calculated using the atomic Mulliken population,⁵³ is also given in table II. The local moment on the Mn atoms ranges between $3.43 \mu_B$ for the ferromagnetic configuration to $3.01 \mu_B$ for the $+ - - +$ configuration. This reduction in the local moment is mainly due to the decrease of the cell volume, and the consequent increase of the hybridization between the Mn- d and As- p orbitals.

In summary these calculations show that the distortion to the B31 structure is caused by an antiferromagnetic alignment of the local magnetic moments in the hexagonal plane.

B. Fit to Heisenberg energy

In order to extract the various exchange parameters, calculations are performed for three different B31 supercells in different local magnetic configurations. These supercells contain 8 Mn atoms, and are obtained by doubling the B31 unit cell along the \mathbf{a} lattice vector (supercell 1), along \mathbf{b} (supercell 2) and along \mathbf{c} (supercell 3). The calculated total energies are then fitted to a model Hamiltonian. The most general form of Hamiltonian able to fit all possible energies for a system of N_s collinear magnetic moments is

$$E_{s_1, s_2, \dots} = E_0 - \sum_{\nu=1}^{N_s} \frac{1}{\nu!} \sum_{j_1} s_{j_1} \sum_{j_2} s_{j_2} \cdots \sum_{j_\nu} s_{j_\nu} J_{j_1, j_2, \dots, j_\nu}, \quad (3)$$

where s_j is the moment at site j (normalized to one), and the J s are coupling parameters. The $J_{i_j, \dots}$ parameters are symmetric under permutations of the indices, and each of the $J_{i_j, \dots}$ is zero if any of the indices i and j are equal.

| | $a(\text{\AA})$ | $b(\text{\AA})$ | $c(\text{\AA})$ | $V(\text{\AA}^3)$ | u/b | v/c | $d_{2,1}(\text{\AA})$ | $d_{2,3}(\text{\AA})$ | $\mu_{\text{Mn}}(\mu_{\text{B}})$ | $\mu_{\text{As}}(\mu_{\text{B}})$ | $E - E_{\text{FM}}(\text{meV})$ |
|------|-----------------|-----------------|-----------------|-------------------|-------|-------|-----------------------|-----------------------|-----------------------------------|-----------------------------------|---------------------------------|
| ++++ | 3.72 | 6.47 | 5.58 | 134.27 | 0.00 | 0.00 | 3.73 | 3.73 | 3.43 | -0.24 | 0 |
| +-+- | 3.56 | 6.18 | 5.81 | 127.93 | 0.00 | 0.00 | 3.56 | 3.57 | 3.10 | 0.00 | 62 |
| +--+ | 3.55 | 6.24 | 5.62 | 124.54 | 0.05 | 0.05 | 3.10 | 4.10 | 3.01 | -0.08 | 17 |
| ---- | 3.62 | 6.29 | 5.70 | 129.83 | 0.04 | 0.04 | 3.12 | 4.17 | 3.33 | -0.03 | 35 |

TABLE II: Relaxed lattice parameters, local magnetic moment of the Mn and As atoms, and total energies per Mn atom for different spin configurations.

The number of independent parameters is therefore 2^{N_s} . Since time reversal symmetry makes the system invariant under a global spin rotation only J s with an even number of indices are not zero and equation (3) reduces to

$$E_{s_1, s_2, \dots} = E_0 - \frac{1}{2} \sum_{i,j} s_i s_j J_{ij} - \frac{1}{4!} \sum_{i,j,k,l} s_i s_j s_k s_l J_{ijkl} - \frac{1}{6!} \sum_{i,j,k,l,m,n} s_i s_j s_k s_l s_m s_n J_{ijklmn} - \dots \quad (4)$$

Here we neglect 4-moment coupling constants J_{ijkl} and higher thus reducing the model to an Ising-type. This approximation neglects the dependence of the moment on each Mn atom as well as the small induced magnetic moment of the As atoms on the orientation of the moments of the surrounding Mn atoms. Furthermore it is assumed that the coupling constants are independent from the angle between the magnetic moments, so that the fit can be extrapolated to vector magnetic moment \mathbf{s}_i to give a Heisenberg type energy

$$E_{\mathbf{s}_1, \mathbf{s}_2, \dots} = E_0 - \frac{1}{2} \sum_{i,j} \mathbf{s}_i \cdot \mathbf{s}_j J_{ij}. \quad (5)$$

In mean field theory the Curie temperature T_C for classical Heisenberg exchanged magnetic moments is

$$k_B T_C = \sum_j J_{0j}/3 = J_0/3, \quad (6)$$

where k_B is the Boltzmann constant. The quantity $J_0 = \sum_j J_{0j}$ is the sum of the exchange coupling constants of a given magnetic moment with all the other moments. In the following sections equation (6) is always used to extract Curie temperatures, although it is well-known that the mean field approximation overestimates T_C .⁵⁴

Calculations are performed for all the independent spin configurations of the supercell 1, and for a randomly chosen subset of those of supercells 2 and 3. 35 different configurations of the magnetic moments are used in total. The energies are then fitted by a least-mean-square fit to the coupling parameters of equation (5). Since the system is metallic with the d -orbitals having finite density of states at the Fermi level, the magnetic interaction

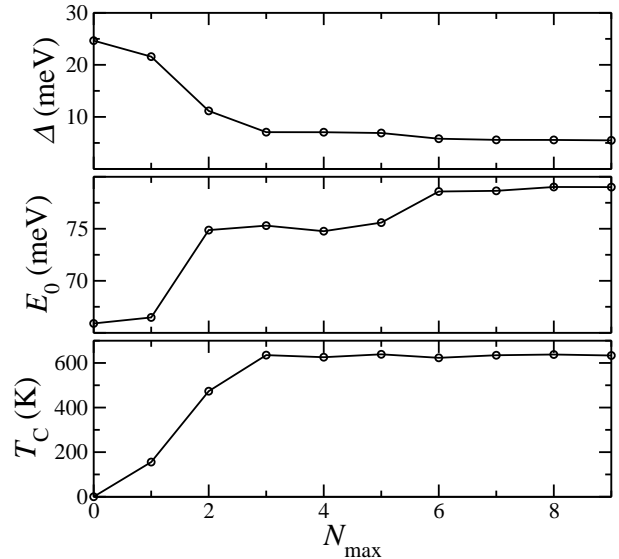


FIG. 7: Variation of the various exchange quantities as function of the number of coupling coefficients N_{max} included in the fit. (a) Standard deviation Δ of the energies resulting from equation (5) as compared to the calculated DFT energies per Mn atom. (b) E_0 per Mn atom (equation (5)), where the zero of energy is chosen as the energy of the ferromagnetic state. (c) Mean field Curie temperature T_C .

is expected to have a long range character. For the chosen supercells it is possible to extract coupling constants up to the ninth nearest neighbor. The lattice parameters used are approximately those for ferromagnetic MnAs in the B8₁ structure at the phase transition temperature $T_p = 318$ K ($a=3.71$ Å, $c/a=1.54$).

We have carefully tested the convergence of our results with the range of the Heisenberg exchange interaction. Figure 7 shows the standard deviation Δ of the energies resulting from equation (5) as compared to the calculated DFT energies per Mn atom, the value of E_0 per Mn atom and the mean field Curie temperature T_C as a function of the number of coupling coefficients N_{max} included in the fit. The standard deviation Δ decays monotonically, remains roughly constant for $N_{\text{max}} \geq 3$, and then reaches a minimum value of around 5 meV for $N_{\text{max}} = 9$. This can be considered as the error resulting from neglecting high moment coupling constants. The value of E_0 changes less over the whole range.

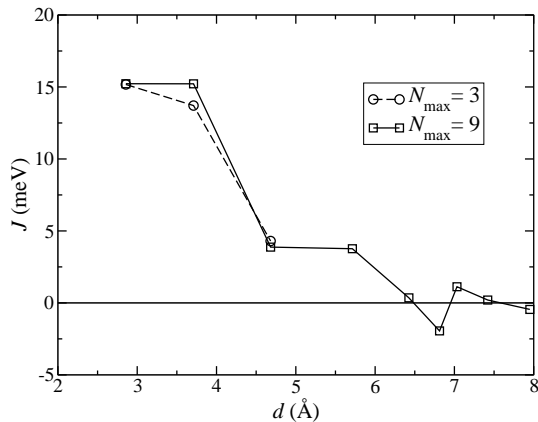


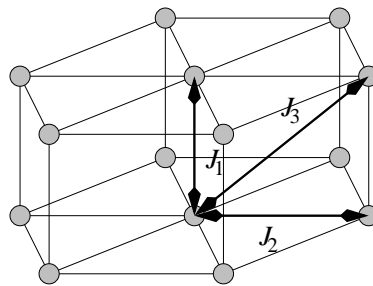
FIG. 8: Exchange coupling parameters for $N_{\max} = 3$ and $N_{\max} = 9$ as a function of the distance between the magnetic moments.

T_C reaches a constant value of approximately 633 K for $N_{\max} \geq 3$. This indicates that the main contribution arises from the first three nearest neighbor coupling constants. The experimental value of T_C for the low temperature phase ranges between $T_p = 318$ K and $T_t = 400$ K. This means that our mean field T_C overestimates the experimental one by about a factor 2.

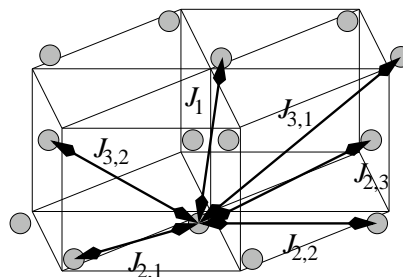
Figure 8 shows the calculated exchange coupling constants as a function of the distance for two different fits counting respectively 3rd and 9th nearest neighbor coupling. The first three exchange constants remain nearly unchanged when going from 3rd to 9th nearest neighbor coupling. Interestingly the coupling parameters are positive and therefore ferromagnetic up to $d \sim 6.5 \text{ \AA}$ (fifth neighbor interaction). In what follows we consider only coupling parameters up to third nearest neighbors, as they give the main contribution to the properties of the material.

C. B8₁ to B31 distortion at T_p

The B8₁ to B31 structural phase transition at T_p is investigated by calculating the Heisenberg coupling constants for different distorted cells. We start from the B8₁ with the experimental lattice parameters near T_p ($a = 3.71 \text{ \AA}$, $b = \sqrt{3} a$, $c = 1.54 a$, $u = v = 0$) and then distort the cell linearly to the B31 structure. The amount of distortion d is given in percent, where $d = 0$ % stands for the lattice parameters of the ferromagnetic B8₁ cell at T_p , and $d = 100$ % for the paramagnetic B31 cell at T_p ($a = 3.676 \text{ \AA}$, $b = 1.01\sqrt{3} a$, $c = 1.556 a$, $u = 0.02 b$, $v = 0.02 c$). Calculations are done for distortions between 0 % and 220 %. Note that the volume decreases with increasing distortion. For these calculations only the supercells 1 and 2 are used with a total of 26 different spin configurations. The standard deviation of the fit is approximately constant for all the distortions and is of the order of 5 meV/Mn.



(a)



(b)

FIG. 9: Schematic representation of the atomic positions of the Mn atoms together with the exchange constants for the B8₁ (a), and the B31 (b) structures.

Figure 9(a) shows the Mn atoms of the B8₁ structure coupled by first (J_1), second (J_2) and third (J_3) nearest neighbor interaction. In the distorted B31 structure the three coupling constants J_1 , J_2 and J_3 are split into six different constants due to symmetry loss. While there is still only one J_1 coupling, the in-plane J_2 splits into three different coupling constants $J_{2,1}$, $J_{2,2}$ and $J_{2,3}$, corresponding to different distances between the Mn atoms in the hexagonal plane (see figure 4). Moreover also the third nearest neighbor coupling J_3 splits into three different constants, although two of them are between Mn atoms separated by approximately the same distance at T_p , and so they are assumed to be identical. Hence J_3 effectively splits only into $J_{3,1}$ and $J_{3,2}$.

Figure 10 shows the calculated values for the exchange parameters as a function of the distortion. For 0% distortion the values of $J_{2,1}$, $J_{2,2}$ and $J_{2,3}$ are approximately equal reflecting the hexagonal symmetry. The values of $J_{3,1}$ and $J_{3,2}$ also should be identical although they differ by about 2 meV (note that in the fit we do not force the

B8₁ symmetry when determining the J s for the undistorted structure). This can be assumed to be the error over the fit. Additional control fits were also performed for different subsets of the 26 spin configurations. The variation over the individual J s was of 20%, whereas the variation of J_0 was always smaller than 6%.

The value of J_1 remains approximately constant for all the distortions, reflecting the fact that the distance between the quasi-hexagonal layers remains roughly constant. In contrast the in-plane J s change and eventually become antiferromagnetic. In particular the coupling becomes strongly antiferromagnetic for $J_{2,1}$, i.e. for those Mn atoms that get closer in the hexagonal plane under distortion. Also $J_{2,3}$, which couples the Mn atoms increasing their separation, is reduced and becomes antiferromagnetic for large distortions. Finally the coupling parameters $J_{3,1}$ and $J_{3,2}$ have only minor changes, with $J_{3,1}$ becoming weakly antiferromagnetic for large distortions.

The evolution of the coupling constants with the distortion explains why for the $+ - + -$ and $+ - - +$ spin configurations (table II), where the spins are antiferromagnetically aligned in the hexagonal plane, the lowest energy is found for the B31 structure. In fact the relaxed structure for both spin configurations is similar to a distortion of about 200 %. At this distortion the in-plane coupling constants $J_{2,1}$ and $J_{2,3}$ become antiferromagnetic, resulting in a reduction of the total energy as compared to the B8₁ structure.

Figure 11(a) shows the relative change of the mean field Curie temperature $T_C(d)/T_C(0)$ for the ferromagnetic state. T_C decreases monotonically with increasing the distortion. For 100 % distortion (B31 structure at T_p) $T_C(100\%)/T_C(0) = 0.67$, demonstrating that when the phase transition from the B8₁ to the B31 structure occurs, the system in the B31 cell is already paramagnetic with very little magnetic order. The experimental Curie temperature T_C^{exp} for the hexagonal cell at $T = T_p$ is not known, since the structure changes.

Figure 11(b) shows the total energy per B31 unit cell as a function of the distortion in the ferromagnetic (FM) and in the $+ - - +$ antiferromagnetic configurations (AF). This latter is the antiferromagnetic configuration giving the lowest total energy at its minimum among all the ones calculated along the considered distortion. The figure also shows the value of E_0 , the energy of the paramagnetic state (see equation (5)). The zero in the energy scale is the energy of the ferromagnetic state for $d = 0$ %.

The ferromagnetic state has its energy minimum for $d = 0$ %, and increases parabolically for increasing distortion. This means that the B8₁ structure is the one with lowest energy in the ferromagnetic state. In contrast the competing antiferromagnetic configuration has a minimum for about 180 % distortion, where the energy is lower than the ferromagnetic phase. The ground state of the system is therefore expected to be ferromagnetic for distortions up to about 100 %, and then to become antiferromagnetic for $d > 180$ %. For distortions in be-

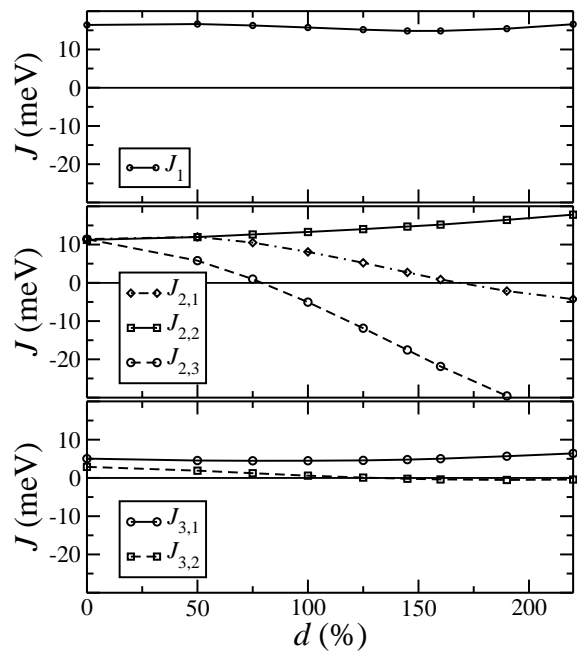


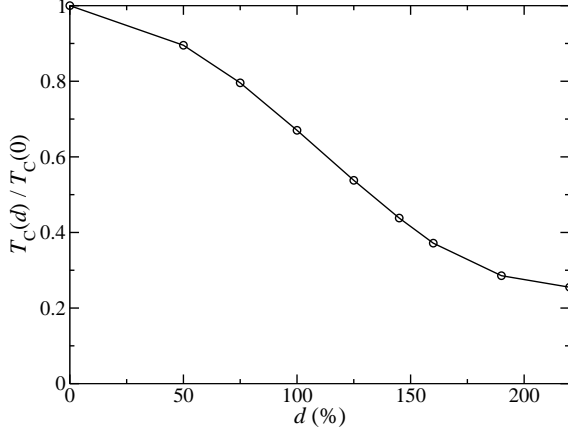
FIG. 10: Evolution of the exchange coupling constants when distorting the unit cell linearly from the B8₁ structure to the B31 structure. $d = 0$ % represents the B8₁ structure at $T_p = 318$ K, $d = 100$ % represents the B31 structure at T_p . A positive (negative) value of J means ferromagnetic (antiferromagnetic) coupling.

tween the ground state is expected to be a non-collinear, canted spin structure.

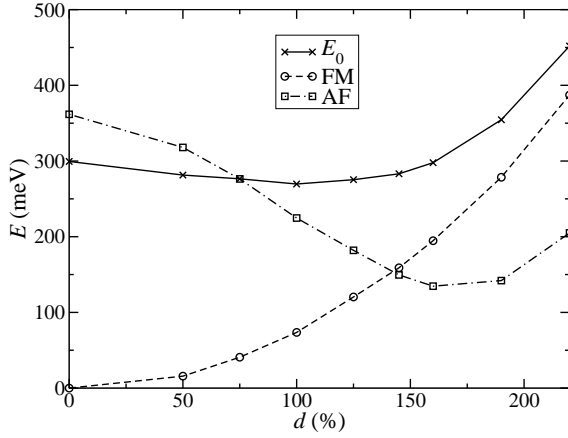
E_0 has a very flat minimum for distorted cells, reflecting the fact that the total energy increases for the ferromagnetic state, but decreases on average for the antiferromagnetic states. The minimum is found to be at about $d \approx 100$ %, which corresponds indeed to the lattice parameters of the paramagnetic state above the phase transition. This explains the structural change from the B8₁ to the B31 structure when the MnAs magnetic state goes from ferromagnetic to paramagnetic. The phase transition at T_p can be seen as a jump from the minimum of the FM curve to the minimum of the E_0 curve.

D. B31 to B8₁ distortion at T_t

For temperature in between T_p and T_t the MnAs crystal structure continuously changes from B31 to B8₁. As mentioned in section II A the phase transition temperature T_t is usually identified as the temperature where the susceptibility and the specific heat have a maximum. This is at about 398 K. However, the distortion disappears at slightly higher temperatures as pointed out in reference [25]. Therefore, since the exact temperature for this second order structural phase transition is not known exactly, we introduce an operative definition and assume that the distortion disappears at a temperature



(a)



(b)

FIG. 11: (a) Relative change of the mean field Curie temperature $(T_C(d) - T_C(0))/T_C(0)$ for the ferromagnetic state. (b) Total energy for one B31 unit cell for the ferromagnetic configuration (FM), for the $+ - - +$ antiferromagnetic configuration (AF), together with E_0 (equation (5)), as a function of the distortion d . $d = 0$ % and $d = 100$ % represent respectively the B8₁ and the B31 phase at $T_p \approx 318$ K.

T_s , at which the slope of the in-plane lattice constant as function of temperature $a(T)$ changes discontinuously (see figure 5). According to figure 5 the lattice constant at T_s is $a(T_s) = \tilde{a} \approx 3.699$ Å, and $(\partial a / \partial T)_{T_s} \approx 0$. At T_t the same lattice parameter is $a(T_t) \approx 3.697$ Å, so that the difference in \tilde{a} is very small.

The main reason for the second order phase transition at high temperatures is related to the lattice thermal expansion. The idea is that upon volume expansion, the ground state of the paramagnetic phase moves towards the hexagonal structure. We verify this hypothesis by calculating the minimum of E_0 (E_0^{\min}) along a distortion of the cell transforming B8₁ to B31. In the calculation

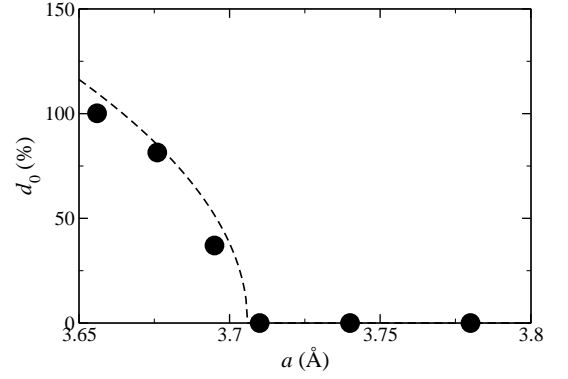


FIG. 12: Distortion d_0 for the minimum of the paramagnetic ground state as a function of the lattice constant a . The dots are calculated values, the dashed line is a fit with equation (7).

the volume of the cell is kept constant and we repeat the calculation for different volumes. This allows us to evaluate both E_0^{\min} and the corresponding distortion as a function of the volume. Since for $T > T_p$ MnAs is always paramagnetic, then the minimum of E_0 corresponds to the stable distortion d_0 at a given volume. In practice the change in volume can be described simply by the change in the planar lattice constant a , since both b/a and c/a do not deviate much from their value at T_p . Thus we always consider $b = \sqrt{3} a$ and $c = 1.556 a$ and the phase transition is investigated as a function of a only.

The equilibrium distortion d_0 as a function of a is presented in figure 12. Indeed the distortion decreases with volume and it disappears for a between $a = 3.695$ Å and $a = 3.71$ Å. Moreover we find 100% distortion for $a \sim 3.66$ Å. These values agree rather well with the experimental ones, where the distortion disappears at about $a(T_s) = 3.699$ Å, and 100% distortion is found at $a(T_p) = 3.673$ Å.

In order to interpret these results consider that the distortion is symmetric for $\pm d$ ($E_0(d) = E_0(-d)$), and therefore E_0 can be expanded in even powers of the distortion $E_0(d) = r_0 + r_1 d^2 + r_2 d^4$. Here r_i are parameters to fit to the DFT calculations. In particular note that r_0 corresponds to the energy of the paramagnetic phase when the crystal is undistorted, i.e. it has the hexagonal structure. In this way the minimum of the $E_0(d)$ curve is obtained for $d_0 = \sqrt{-\frac{r_1}{2r_2}}$. For small distortions the parameters r_1 and r_2 can be further expanded around \tilde{a} as $r_1 = r_{1,1}(a - \tilde{a})$ and $r_2 = r_{2,0} + r_{2,1}(a - \tilde{a}) + r_{2,2}(a - \tilde{a})^2$. The calculated values for the leading terms are $\tilde{a} = 3.706$ Å, $r_{1,1} = 62.4 \cdot 10^{-3}$ meV/Å and $r_{2,0} = 1.29 \cdot 10^{-7}$ meV, (d is given in percent). The equilibrium distortion d_0 up to first order in a is then

$$d_0(a) = \gamma \sqrt{\frac{\tilde{a} - a}{\tilde{a}}} \Theta(\tilde{a} - a), \quad \gamma = \sqrt{\tilde{a} \frac{r_{1,1}}{2 r_{2,0}}}, \quad (7)$$

where $\Theta(x)$ is the Heaviside function. With the values

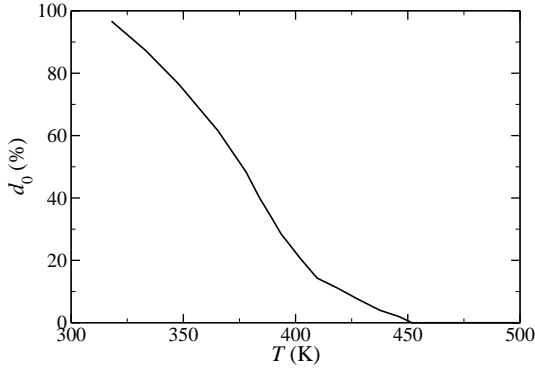


FIG. 13: Distortion d_0 for the minimum of the paramagnetic ground state as a function of temperature calculated with equation (7) (with $\gamma = 1184$ and $\tilde{a} = 3.699$) using $a(T)$ taken from figure 5.

of \tilde{a} , $r_{1,1}$ and $r_{2,0}$ given above $\gamma = 947$ is obtained. The resulting distortion is presented in figure 12.

Interestingly if we use the equation (7) to fit the experimentally determined distortions at $a(T_s) = 3.699\text{\AA}$ ($d_0 = 100\%$) and $a(T_p) = 3.673\text{\AA}$ ($d_0 = 0$), we obtain $\gamma = 1184$ and $\tilde{a} = 3.699$, both in good agreement with our calculated values. This suggests that the main effects of the distortion to the B31 structure arise from the atomic displacement from the symmetry positions, and that small changes of the ratio of the lattice vectors, neglected in our calculations, play only a secondary role. Using the values $\gamma = 1184$ and $\tilde{a} = 3.699$ of the two parameters the evolution of the distortion as a function of temperature T can be obtained by inserting the data for $a(T)$ from figure 5 in equation (7). The result is shown in figure 13. It agrees well with the experimental result (see figure 3 in reference 10). The main difference however is that in reference 10 the distortion d_0 becomes zero at 398 K, whereas in our results this happens only at 450 K. This is due to our choice of $T_s = 450$ K, which by definition sets the temperature where the distortion disappears. Close to the phase transition temperature fluctuations play an important role, so that for very small distortions close to the phase transition the description may not be valid.

By using the computed values of r_0 , r_1 and r_2 the minimum of E_0 ($E_0^{\min} = E_0(d = d_0)$) is calculated as a function of the volume of the unit cell, and it is shown in figure 14 together with r_0 . Recalling that r_0 is the energy of the paramagnetic hexagonal phase, it also can be expanded as function of the lattice constant $r_0 = \epsilon_0 + \epsilon_1 (a - a_0)^2$, where a_0 is the equilibrium lattice constant of the hexagonal phase. This, combined with equation (7), gives an expression for the energy minimum as a function of the lattice constant a

$$E_0^{\min}(a) = \epsilon_0 + \epsilon_1 (a - a_0)^2 - \epsilon_2 (a - \tilde{a})^2 \Theta(\tilde{a} - a),$$

$$\epsilon_2 = \frac{r_{1,1}^2}{4r_{2,0}} = 7546 \frac{\text{meV}}{\text{\AA}^2},$$
(8)

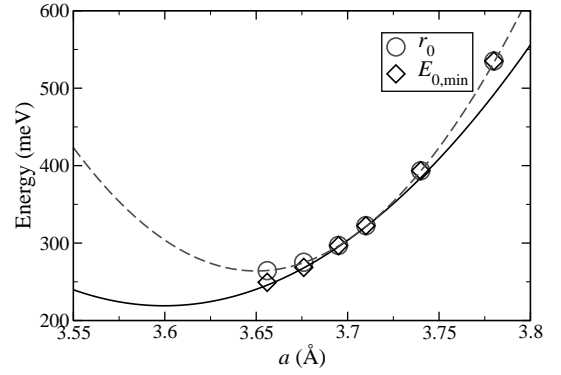


FIG. 14: Energy expansion coefficient r_0 and $E_{0,\min}$ as function of the lattice constant. The dashed line shows $\epsilon_0 + \epsilon_1 (a - a_0)^2$, the solid line shows $\epsilon_0 + \epsilon_1 (a - a_0)^2 - \epsilon_2 (a - \tilde{a})^2$ (see equation (8)).

where ϵ_0 , ϵ_1 and a_0 are to be fitted from the calculations of r_0 (figure 14). The fitted values are $\epsilon_0 = 264$ meV, $\epsilon_1 = 15935$ meV/ \AA^2 and $a_0 = 3.65$ Å. From the equation (8) the energy minimum is easily found

$$a_{\min} = a_0 \left(1 - \frac{\epsilon_2}{\epsilon_1 - \epsilon_2} \frac{\tilde{a} - a_0}{a_0} \right),$$
(9)

and by using the calculated parameters we estimate $a_{\min} = 3.60$ Å. Since $a_{\min} < a_0$, we derive the important result that the distortion allows the volume to be further reduced as compared to the hexagonal phase. Furthermore the curvature of the energy as a function of a is

$$\frac{\partial^2 E_0^{\min}(a)}{\partial a^2} = 2\epsilon_1 - 2\epsilon_2 \Theta(\tilde{a} - a),$$
(10)

which is also reduced by a factor $2\epsilon_2$ when the structure is distorted.

The effect of the thermal expansion on the lattice parameter can now be modeled as a temperature dependent position of a_0 , $a_0 = a_0(T)$. The change of the lattice constant with temperature for the distorted phase can therefore be written as

$$\frac{\partial a_{\min}}{\partial T} = \frac{\epsilon_1}{\epsilon_1 - \epsilon_2} \frac{\partial a_0}{\partial T}$$
(11)

Since ϵ_2 is smaller than ϵ_1 the lattice expands with temperature faster for the distorted phase than for the undistorted phase. If the calculated values for ϵ_1 and ϵ_2 are used the ratio $\epsilon_1/(\epsilon_1 - \epsilon_2)$ is found to be 1.90, which agrees well with the value of 2.25 extracted from figure 5. Near the phase transition, i.e. where $d \approx 0$, phononic effects due to the different curvatures of the energy and fluctuations should be considered. It is especially interesting that the change of the lattice constant with the temperature goes to zero near the phase transition temperature.

In the same way as E_0 also T_C can be expanded as a function of the lattice constant and of the distortion

$$T_C(a, d) = T_C(\tilde{a}) \left[1 + K_v \frac{a - \tilde{a}}{\tilde{a}} - K_d d^2 \right], \quad (12)$$

where K_v and K_d are parameters, and $T_C(\tilde{a})$ is the Curie temperature for the cell with lattice parameter \tilde{a} and where the atoms are in the hexagonal positions. The parameters are fitted by least mean squares to the calculated values of T_C obtained for six lattice constants ranging between 3.656 Å and 3.78 Å and for different distortions. We obtain $T_C(\tilde{a})=573$ K, $K_v = 6.80$ and $K_d = 2.62 \cdot 10^{-5}$. At $d = 100\%$ the relative change of the Curie temperature is $T_C(\tilde{a}, d = 100\%)/T_C(\tilde{a}) = 0.74$ and corresponds roughly to the value of figure 11(a). In this case it is slightly larger due to the fact that the volume is kept constant, whereas for the calculations of figure 11(a) it shrinks with increasing the distortion.

Next we calculate the dependence of the magnetic moment on the distortion and on the unit cell volume. The dependence is again expanded to lowest order in a and d

$$\mu(a) = \mu(\tilde{a}) \left[1 + \alpha_\mu \frac{a - \tilde{a}}{\tilde{a}} + \alpha_{\mu,d} d^2 \right]. \quad (13)$$

We now have different ways of extracting the magnetic moment of the Mn atoms from our DFT calculations. One possibility is to take the total moment of the cell for the ferromagnetic spin configuration and divide it by the number of Mn atoms. In this way however the small induced moments of the As atoms are subtracted from the moment on the Mn. A second possibility is to take the average Mulliken spin population for the Mn atoms. The advantage of this method is that also antiferromagnetic configurations can be used to determine the average moment, and the induced moments of the As atoms are accounted for. The drawback however is that Mulliken populations are somewhat arbitrary as they depend on the basis set.

By setting \tilde{a} to 3.699 Å, the values obtained using the cell moment are $\mu(\tilde{a}) = 3.28 \mu_B$, $\alpha_\mu=3.28$ and $\alpha_{\mu,d}=1.15 \cdot 10^{-6}$. Similarly from the average Mulliken population over all the magnetic configurations we obtain $\mu(\tilde{a})=3.42 \mu_B$, $\alpha_\mu=3.48$, and $\alpha_{\mu,d} \approx 0$. These results are rather similar to each other. Our analysis shows that the change of the magnetic moment is mainly due to the change in volume, whereas the distortion has basically no effect.

E. Small distortions of the B8₁ structure

In this section the dependence of T_C on the individual lattice parameters and on the distances between the atoms is investigated for the B8₁ structure. Our approach is to distort the cell orthorhombically but to leave the atoms in their high symmetry positions. Apart from

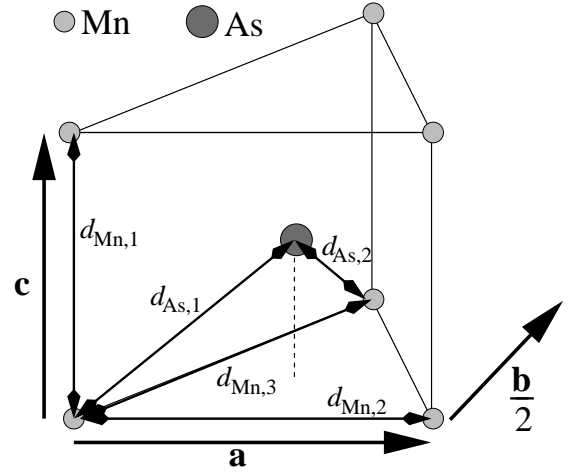


FIG. 15: Diagram of the positions of Mn and As atoms in orthorhombic MnAs.

a general understanding of the phase diagram of MnAs this analysis is useful for predicting the behavior of MnAs when grown on a substrate. For instance when grown on GaAs(001) the substrate induces strain in MnAs, and the unit cell is slightly orthorhombically distorted.¹ This distortion does not correspond to the orthorhombic B31 structure, since the atoms do not move out of the high symmetry positions. Moreover different growth orientations are possible, and the Curie temperature varies accordingly.⁷ In addition reference [8] presents experimental results showing that the phase transition temperature T_p changes when strain is applied to the MnAs film. In that article we have compared our theoretical predictions for the dependence of T_p on the lattice distortion with the experimental findings. In this section we refine and expand our previous analysis.

When the cell is orthorhombically distorted the first three nearest neighbor coupling constants split into five different constants, corresponding to the ones of the B31 cell (figure 9), and with the only exception that now $J_{2,1} = J_{2,3}$. The number of total energy calculations for the fit of the coupling parameters is 16. The change of T_C for each different distortion can be expressed as a function of the change of each single Mn-Mn and Mn-As distance in the unit cell. This gives

$$\frac{\delta T_C}{T_C} = \frac{\delta J_0}{J_0} = \sum_{\mu=1}^5 K_\mu N_\mu \frac{\delta d_\mu}{d_\mu}, \quad (14)$$

where the sum goes over all five independent distances in the orthorhombic unit cell as defined in figure 15. The dependence on the angles between the atoms is neglected. N_μ are the multiplicities of each distance d_μ within one unit cell, and have the values $N_{Mn,1} = 4$, $N_{Mn,2} = 4$, $N_{Mn,3} = 8$, $N_{As,1} = 4$, $N_{As,2} = 8$. For the evaluation of the coefficients K_μ , 21 different distortions are considered, including changes of volume, changes of the ratio of the different axes and different displacements of

the As atoms. For all the distortions the orthorhombic symmetry however was preserved. The best fit for K_μ gives

$$\begin{aligned} K_{\text{Mn},1} &= 6.6, \quad K_{\text{Mn},2} = 6.2, \quad K_{\text{Mn},3} = 5.9, \\ K_{\text{As},1} &= -7.5, \quad K_{\text{As},2} = -7.5. \end{aligned} \quad (15)$$

The values of $K_{\text{Mn},1}$ and $K_{\text{Mn},2}$ are almost identical, as one should expect from the symmetry and similarly for $K_{\text{As},1}$ and $K_{\text{As},2}$.

Equation (14) describes the fact that the change of T_C is the result of an interplay between the change of the Mn-Mn and Mn-As distances. The calculated K_μ show that, while an increase in the distance between Mn atoms increases T_C , an increase of the Mn-As distance decreases it. However note that the two distances can not be changed independently, thus the net change in T_C depends on the details of the distortion.

J_0 can also be expanded over the orthorhombic lattice parameters

$$\frac{\delta J_0}{J_0} = \sum_{i=1}^3 K_i \frac{\delta a_i}{a_i}, \quad \text{with } K_i = \sum_{\mu=1}^5 K_\mu N_\mu \frac{a_i}{d_\mu} \frac{\partial d_\mu}{\partial a_i}, \quad (16)$$

where $a_1 = a$, $a_2 = b$ and $a_3 = c$. The change of the distances between Mn and As atoms is not exactly known for the orthorhombic cell. However it is easy to show that to first order the position of the As atom in the cell does not influence J_0 , since up to first order $\delta d_{\text{As},2} = 2\delta d_{\text{As},1}$ when moving the As atom inside the cell. Therefore the As atoms can be assumed to remain in the high symmetry position. Assuming now $K_2 = K_3$ and $K_4 = K_5$ (as imposed by symmetry), the general form of the K_i is

$$\begin{aligned} K_a &= K_b = 6K_2 + \frac{96K_4}{16 + 3\tilde{c}^2}, \\ K_c &= 4K_1 + \frac{36K_4\tilde{c}^2}{16 + 3\tilde{c}^2}, \end{aligned} \quad (17)$$

where $\tilde{c} = c/a$. Using the average between K_2 and K_3 and $\tilde{c} = 1.533$ this gives

$$K_a = K_b = 4.9, \quad K_c = -1.0. \quad (18)$$

Our results clearly show that stretching the unit cell along the basal plane raises T_p (since $K_a > 0$), while stretching along the c -axis lowers T_p ($K_c < 0$). An increase of the volume without distorting the cell results in an increase of the ferromagnetic exchange interactions and therefore of T_C , since K_a is positive and larger in magnitude than K_c . If the cell changes only its volume the expansion corresponds to the one of equation (12) with a factor $K_v = 2K_a + K_c = 8.8$. These results differ slightly from the ones given in reference [8], since in that case we did not constrain K_a to be equal to K_b .

IV. DISCUSSION

A. Curie temperature and susceptibility

It is now possible to analyze two peculiar properties of MnAs. The first is the anomalous behavior of the susceptibility χ as a function of temperature between T_p and T_t . The second is the fact that although the Curie temperature for ferromagnetic MnAs has to be larger than T_p , the T_C extrapolated from the susceptibility above T_t is only 285 K.¹³ In this section both these features are explained using the dependence of the susceptibility on the Curie temperature ($\chi = \chi(T_C)$), and the strong dependence of the Curie temperature on the lattice parameters $T_C = T_C(a, b, c, d)$. $T_C(T)$ and $\chi(T)$ are therefore determined using the experimentally measured temperature dependence of the lattice vectors $a(T), b(T)$ and $c(T)$ and of the distortion $d(T)$. This analysis also provides a tool for extracting the parameters K_v and K_d from experimental data.

By generalizing the equations (12) and (16) the Curie temperature $T_C(a, b, c, d)$ can be written as

$$T_C(a, b, c, d) = T_{C,0} \left[1 + K_a \left(\frac{a - \tilde{a}}{\tilde{a}} + \frac{b - \tilde{b}}{\tilde{b}} \right) + K_c \frac{c - \tilde{c}}{\tilde{c}} - K_d d^2 \right], \quad (19)$$

where we use the fact that $K_a = K_b$. We take the values for K_a and K_c from equation (18), $K_d = 2.62 \cdot 10^{-5}$ and $T_{C,0} = T_C(\tilde{a}) = 573$ K are those calculated in section III D. The reference lattice parameters are chosen to be the lattice vectors at T_s ($\tilde{a} = 3.699$ Å, $\tilde{b} = \sqrt{3} \tilde{a}$, $\tilde{c} = 1.56 \tilde{a}$).

Similarly to the Curie temperature also the susceptibility is calculated in the mean field approximation. This is justified for $T \gg T_C$, a condition which is satisfied for paramagnetic MnAs. The molar susceptibility χ_M is then given by

$$\begin{aligned} \chi_M^{-1} &= \frac{1}{C_0} (T - T_C), \\ C_0 &= \frac{N_A \mu_B^2 g^2}{3k_B} s(s+1). \end{aligned} \quad (20)$$

N_A is the Avogadro's number, $g \approx 2$ is the Lande's factor for the free electron spin, k_B is the Boltzmann constant and s is the atomic total spin. Note that the susceptibility has an additional implicit temperature dependence since T_C and s depend on the temperature through the lattice distortion. However in what follows we neglect the dependence of s on the lattice parameters so that C_0 is constant over all temperature. An analysis performed by relaxing this approximation gives similar results.

Similarly to section III D the model is further simplified by assuming that b/a and c/a are constant above T_p . As indicated in equation (7) d then is a function of the lattice constant, $d(a) = \gamma \sqrt{(\tilde{a} - a)/\tilde{a}} \Theta(\tilde{a} - a)$. Moreover we

have shown that the experimental distortion as function of the lattice constant is well reproduced when $\gamma = 1184$. Therefore it is now possible to express T_C and χ_M^{-1} as a function of the lattice constant a only

$$\chi_M^{-1}(a) = \frac{1}{C_0} \left[T - T_{C,0} \left(1 + (K_v + K_d \gamma^2 \Theta(\tilde{a} - a)) \frac{a - \tilde{a}}{\tilde{a}} \right) \right], \quad (21)$$

where $K_v = 2K_a + K_c = 8.8$. This equation shows that if the lattice expands strongly with temperature χ_M^{-1} decreases.

For temperatures between T_p and about 390 K, as well as above T_s , a increases approximately linearly with temperature (see figure 5) and can therefore be written as

$$a(T) = a(T_0) \left[1 + \alpha \frac{T - T_0}{T_0} \right], \quad (22)$$

where the experimental values for the coefficients are $T_{0,+} = T_s = 452$ K, $a(T_s) = \tilde{a} = 3.699$ Å and $\alpha_+ = 0.0126$ for temperatures above T_s (the index “+” denotes the high temperature region above T_s), and $T_{0,-} = T_p = 318$ K, $a(T_p) = 3.673$ and $\alpha_- = 0.0284$ for temperatures between T_p and about 390 K (the index “-” denotes the intermediate temperature region). By inserting equation (22) into equation (21) we obtain for the high temperature region above T_s

$$\chi_M^{-1}(T) = \frac{1}{C_{\text{eff}}}(T - T_{C,\text{eff}}), \quad (23)$$

with

$$C_{\text{eff}} = \frac{1}{1 - K_v \alpha_+ \frac{T_{C,0}}{T_s}} C_0, \quad (24)$$

$$T_{C,\text{eff}} = \frac{1 + K_v \alpha_+}{1 - K_v \alpha_+ \frac{T_{C,0}}{T_s}} T_{C,0}.$$

$T_{C,\text{eff}}$ and C_{eff} are the experimentally accessible quantities for the high temperature susceptibility, and due to the expansion of the lattice they are different from $T_{C,0}$ and C_0 . The experimentally measured values are $T_{C,\text{eff}} = 285$ K and $C_{\text{eff}} = 3.12 \cdot 10^{-5} \text{ m}^3 \text{ K}$,¹⁴ which corresponds to an effective magnetic moment of $3.57 \mu_B$. From C_{eff} and $T_{C,\text{eff}}$ the values of $T_{C,0} = T_C(\tilde{a})$ and C_0 can now be obtained

$$C_0 = \frac{1 - K_v \alpha_+}{1 - K_v \alpha_+ \left(1 - \frac{T_{C,\text{eff}}}{T_s} \right)} C_{\text{eff}}, \quad (25)$$

$$T_{C,0} = \frac{1}{1 - K_v \alpha_+ \left(1 - \frac{T_{C,\text{eff}}}{T_s} \right)} T_{C,\text{eff}}.$$

All the variables on the right hand side of equation (25) can be obtained from experiment except K_v . For small K_v the difference between $T_{C,0}$ and $T_{C,\text{eff}}$ is proportional

to K_v . Since T_s is larger than the experimental value of $T_{C,\text{eff}}$ the effect of the thermal expansion of the hexagonal structure is a reduction of the slope of the inverse susceptibility as a function of temperature, as well as a reduction of the extrapolated Curie temperature as compared to the real Curie temperature.

In the region where linear expansion holds the slope of the inverse susceptibility above T_t is

$$\frac{\partial \chi_{M,+}^{-1}}{\partial T} = \frac{1}{C_0} \left(1 - K_v \alpha_+ \frac{T_{C,0}}{T_t} \right), \quad (26)$$

whereas for in the intermediate temperature region above T_p it is

$$\frac{\partial \chi_{M,-}^{-1}}{\partial T} = \frac{1}{C_0} \left(1 - (K_v + K_d \gamma^2) \alpha_- \frac{a_0 T_{C,0}}{\tilde{a} T_{0,-}} \right). \quad (27)$$

In both regions there is a reduction of the slope due to the expansion of the lattice. However the reduction is much larger for $\chi_{M,-}$ than for $\chi_{M,+}$, since there is the additional term proportional to K_d due to the distortion, and also $\alpha_- > \alpha_+$. As a rough approximation it can be assumed that $(a_0 T_{C,0})/(\tilde{a} T_{0,-}) \approx 1$, so that $\frac{\partial \chi_{M,-}^{-1}}{\partial T}$ becomes negative for

$$(K_v + K_d \gamma^2) \alpha_- > 1. \quad (28)$$

The values of α and γ are determined experimentally and describe how the structure changes with temperature, whereas K_v and K_d describe how T_C varies for distorted cells. By using our calculated values for K_v and K_d we obtain $(K_v + K_d \gamma^2) \alpha_- = 1.29$. This is indeed larger than one. Therefore we do predict a negative slope for the inverse susceptibility in the intermediate temperature region.

Finally we extract the values for K_v and K_d from the experimental behavior of the Curie temperature. Since the ratio between K_a and K_c can not be obtained from the thermal properties of MnAs, it is therefore assumed that $K_c/K_a = -1/4.9 = -0.2$ is fixed and corresponds to our calculated value. For the hexagonal cell ($d = 0$) the equation (19) reads

$$T_C(a, c) = T_{C,0} \left[1 + K_v \left(k_a \frac{a - \tilde{a}}{\tilde{a}} + k_c \frac{c - \tilde{c}}{\tilde{c}} \right) \right], \quad (29)$$

where $k_a = 2/(2 + K_c/K_a) = 1.11$ and $k_c = (K_c/K_a)/(2 + K_c/K_a) = -0.11$. This has to be valid for all temperatures where the cell is hexagonal, therefore it can not be assumed that the ratio between c and a is constant since it changes abruptly from 1.533 to 1.556 at T_p . By using the expression for $T_{C,0}$ from equation (25) we obtain K_v

$$K_v = \frac{\frac{T_C(a,c)}{T_{C,\text{eff}}} - 1}{\alpha_+ \left(\frac{T_C(a,c)}{T_{C,\text{eff}}} - \frac{T_C(a,c)}{T_s} \right) + k_a \frac{a - \tilde{a}}{\tilde{a}} + k_c \frac{c - \tilde{c}}{\tilde{c}}}. \quad (30)$$

As reference Curie temperature the extrapolated value to room temperature is used, which can be estimated to be about $T_C(a = 3.724 \text{ \AA}, c = 1.533a) = 360 \text{ K}$. By inserting the experimental values for the parameters on the right hand side of the equation (30) we obtain $K_v = 18.1$. This is about twice as big as our predicted value. The disagreement may be due to the fact that the ratio between K_c and K_a has been fixed for our calculated value. By inserting this value for K_v in equation (25) we obtain $T_{C,0} = 311 \text{ K}$, the Curie temperature for the lattice parameters at $T = T_s$.

In order to extract K_d from experiments we use the relative change in the slope of the inverse susceptibility around T_t . This is, according to the equations (26) and (27),

$$\frac{\frac{\partial \chi_{M,+}^{-1}}{\partial T} - \frac{\partial \chi_{M,-}^{-1}}{\partial T}}{\frac{\partial \chi_{M,+}^{-1}}{\partial T}} = 1 - \frac{1 - (K_v + K_d \gamma^2) \alpha_- \frac{a_0}{a} \frac{T_{C,0}}{T_0}}{1 - K_v \alpha_+ \frac{T_{C,0}}{T_t}}, \quad (31)$$

and increases with increasing K_v and K_d . All the variables in this equation can be derived from the experimental measurements, except K_v and K_d . Experimentally different values are found for the relative change of the slope (left hand side of equation (31)).^{25,55,56,57} These are all of the order of 1.44. By using this value for the relative change of the slope and the previously calculated value $K_v = 18.1$, K_d is found to be $1.78 \cdot 10^{-5}$. This value agrees approximately with our predicted value of $2.62 \cdot 10^{-5}$.

In conclusion the table III summarizes the parameters calculated in this work, by comparing our *ab initio* results obtained from the DFT calculations and the Heisenberg model, with the results obtained by fitting to the experimental data. In general there is a fair agreement, although the the DFT results underestimate K_v and overestimate K_d .

| | $T_{C,0}$ (K) | K_d (10^{-5}) | K_v | K_a | K_c | γ | \tilde{a} (\AA) |
|-----|------------------|------------------------|-------|-------|-------|----------|------------------------------|
| DFT | 579 | 2.62 | 8.8 | 4.9 | -1.0 | 947 | 3.706 |
| FIT | 311 | 1.78 | 18.1 | 10.1 | -2.1 | 1184 | 3.699 |

TABLE III: Main parameters used in the description of the phase diagram of MnAs. We compared results obtained from *ab initio* calculations and Heisenberg model (DFT), with those of the best fit to the experimental properties (FIT).

B. Phase diagram

It is now possible to draw a qualitative description of the phase diagram of MnAs (see figure 2). Since the magnetic interactions are strongly dependent on the volume, the effects of the thermal expansion of the lattice

are important. First the state of MnAs at zero pressure is considered. For $P = 0$ and temperatures below 155 K both ferromagnetic and canted spin structures can be stabilized. The ground state is the ferromagnetic B8₁ structure, however also the B31 structure is stable, because at these low temperatures the thermal energy is not large enough to induce a phase transition from a canted spin structure to a ferromagnetic one. As the temperature increases above 155 K the thermal fluctuation may induce the phase transition, and therefore only the ferromagnetic state survives.

As the temperature is further increased and the system becomes paramagnetic, the B31 structure becomes the stable state, as described in section III C (figure 11(b)). MnAs then remains paramagnetic for all temperatures, but because of the thermal expansion the orthogonal distortion decreases, until it vanishes when a critical volume is reached (see figure 12). Then the volume becomes large enough to stabilize the B8₁ structure even for a paramagnetic state, leading to the second structural phase transition at T_t .

As pressure is applied to the system the volume is reduced and thus the ferromagnetic exchange interaction decreases. Therefore T_p decreases with pressure, while T_t increases. At a temperature of approximately 230 K the ferromagnetic state is stable up to a pressure of 2kbar. For high pressures above 2.5-4 kbar the volume is small enough that canted spin structures become the ground state. The temperature at which these states become paramagnetic is approximately 230 K. It increases slightly with pressure, reflecting the fact that the antiferromagnetic interaction increases as the volume is reduced.

V. CONCLUSIONS

We have investigated by means of *ab initio* electronic structure calculations the magneto-structural properties of MnAs. The stable structure for the ferromagnetic state is found to be the B8₁ structure. However if antiferromagnetic alignment in the hexagonal plane is imposed the B31 structure becomes more stable. By fitting the DFT total energies of different magnetic configurations to a Heisenberg type energy it is shown that the main contributions to the physical properties originate from the exchange coupling parameters up to 3rd nearest neighbor. The Curie temperature was calculated in the mean field approximation, with values approximately twice as large as the experimental ones.

The main assumption of the phenomenological model of Bean and Rodbell¹¹ that the ferromagnetic exchange coupling parameters increase when the volume is increased has been confirmed (equation (18)) using this analysis. However it has been shown that the exchange interactions depend not only on the volume, but that the orthogonal distortion to the B31 structure plays an important role. For the experimentally observed distor-

tions some of the in-plane exchange coupling coefficients become antiferromagnetic. This is the reason for the stability of the B31 structure for those configurations of the magnetic moments that have an antiferromagnetic component in the hexagonal plane. Different canted spin structures are expected to minimize the energy for different distortions, since there are both positive and negative exchange coefficients depending on the amount of distortion of the B31 structure.

Furthermore it has been shown that for paramagnetic states the B31 structure is stable at small volumes, while the B8₁ structure is stable above a critical lattice constant of about 3.7 Å. This explains the second order phase transition at T_t , since at that temperature the lattice constant crosses this critical value.

The Curie temperature has been expanded as a function of the lattice vectors and of the amount of distortion. An increase in the volume leads to an enhancement of the Curie temperature, while an increase of the distortion leads to a reduction. With these results in hand the increase of the susceptibility between T_p and T_t has

been explained as the result of the increase of the Curie temperature due to the change of the structure from the B31 to the B8₁ and to the increase of the volume. By using the experimental variation of the lattice parameters with increasing temperature the susceptibility is indeed found to increase between T_p and T_t .

A fit of the dependence of the Curie temperature on the lattice parameters to best reproduce the experimental behavior is also given. The calculated values agree within a factor of two with the values obtained by the *ab initio* calculations. Our results are in agreement with the phenomenological models based on the Bean Rodbell idea. But now the various parameters used are derived from first principles and therefore validated.

Acknowledgments

We acknowledge the financial support from SFI (grant number SFI02/IN1/I175).

-
- ¹ A. K. Das, C. Pampuch, A. Ney, T. Hesjedal, L. Däweritz, R. Koch, and K. H. Ploog, Phys. Rev. Lett. **91**, 087203 (2003).
 - ² K. Akeura, M. Tanaka, M. Ueki, and T. Nishinaga, Appl. Phys. Lett. **67**, 3349 (1995).
 - ³ K. H. Ploog, Physica E **24**, 101 (2004).
 - ⁴ J. H. Song, J. J. Lee, Y. Cui, J. B. Ketterson, and S. Cho, Appl. Phys. Lett. **85**, 4079 (2004).
 - ⁵ J. H. Song, Y. Cui, J. J. Lee, Y. Kim, J. B. Ketterson, and S. Cho, J. Appl. Phys. **95**, 7288 (2004).
 - ⁶ M. Ramsteiner, H. Y. Hao, A. Kawaharazuka, H. J. Zhu, M. Kästner, R. Hey, L. Däweritz, H. T. Grahn, and K. H. Ploog, Phys. Rev. B **66**, 081304(R) (2002).
 - ⁷ M. J. S. P. Iikawa, F. Brasil, O. D. D. Couto, C. Adriano, C. Giles, and Däweritz, Appl. Phys. Lett. **85**, 2250 (2004).
 - ⁸ F. Iikawa, M. J. S. P. Brasil, C. Adriano, O. D. D. Couto, C. Giles, P. V. Santos, L. Däweritz, I. Rungger, and S. Savito, Phys. Rev. Lett. **95**, 077203 (2005).
 - ⁹ J. Mira, F. Rivadulla, J. Rivas, A. Fondado, T. Guidi, R. Caciuffo, F. Carsughi, P. G. Radaellil, and J. B. Goodenough, Phys. Rev. Lett. **90**, 097203 (2003).
 - ¹⁰ T. Suzuki and H. Ido, J. Phys. Soc. Jpn. **51**, 3149 (1982).
 - ¹¹ C. P. Bean and D. S. Rodbell, Phys. Rev. **126**, 104 (1962).
 - ¹² R. W. De Blois and D. S. Rodbell, Phys. Rev. **130**, 1347 (1963).
 - ¹³ J. B. Goodenough and J. A. Kafalas, Phys. Rev. **157**, 389 (1967).
 - ¹⁴ N. Menyuk, J. A. Kafalas, K. Dwight, and J. B. Goodenough, Phys. Rev. **177**, 942 (1969).
 - ¹⁵ F. Groonvold, S. Snildal, and E. F. Westrum Jr., Acta Chem. Scand. **24**, 285 (1970).
 - ¹⁶ A. Zieba, K. Selte, A. Kjekshus, and A. F. Andresen, Acta Chem. Scand. **A32**, 173 (1978).
 - ¹⁷ A. Zieba, Y. Shapira, and S. Foner, Phys. Lett. **91A**, 243 (1982).
 - ¹⁸ V. A. Chernenko, L. Wee, P. G. McCormick, and R. Street, J. Appl. Phys. **85**, 7833 (1999).
 - ¹⁹ F. Ishikawa, K. Koyama, K. Watanabe, and H. Wada, Jpn. J. Appl. Phys. **42**, L918 (2003).
 - ²⁰ L. H. Schwartz, E. L. Hall, and G. P. Felcher, J. Appl. Phys. **42**, 1621 (1971).
 - ²¹ J. B. Forsyth, S. J. Pickart, and P. J. Brown, Proc. Phys. Soc. **88**, 333 (1966).
 - ²² R. Koch, C. Pampuch, H. Yamaguchi, A. K. Das, A. Ney, L. Däweritz, and K. H. Ploog, Phys. Rev. B **70**, 092406 (2004).
 - ²³ B. T. M. Willis and H. P. Rooksby, Proc. Phys. Soc. (London) **B67**, 290 (1954).
 - ²⁴ R. H. Wilson and J. S. Kasper, Acta Crystallogr. **17**, 95 (1964).
 - ²⁵ L. Pytlik and A. Zieba, J. Magn. Magn. Mater. **51**, 199 (1985).
 - ²⁶ C. Kittel, Phys. Rev. **120**, 335 (1960).
 - ²⁷ D. S. Rodbell and C. P. Bean, J. Appl. Phys. **33**, 1037 (1962).
 - ²⁸ K. Bärner, E. A. Zavadskii, and D. Y. Suminov, Phys. Stat. Sol. B **214**, 411 (1999).
 - ²⁹ S. Haneda, N. Kazama, Y. Yamaguchi, and H. Watanabe, J. Phys. Soc. Jpn. **42**, 31 (1977).
 - ³⁰ s. Haneda, N. Kazama, Y. Yamaguchi, and H. Watanabe, J. Phys. Soc. Jpn. **42**, 1212 (1977).
 - ³¹ T. Kato, K. Nagai, and T. Aisaka, J. Phys. C: Sol. Stat. Phys. **16**, 3183 (1983).
 - ³² I. M. Vitebskii, V. I. Kamenev, and D. A. Yablonskii, Sov. Phys. Solid State **23**, 121 (1981).
 - ³³ S. K. Asadov, E. A. Zavadskii, V. I. Kamenev, E. P. Stefanovskii, A. L. Sukstanskii, and B. M. Todris, Phys. Solid State **42**, 1696 (2000).
 - ³⁴ V. I. Val'kov and A. V. Golovchan, Low Temp. Phys. **30**, 711 (2004).
 - ³⁵ K. Motizuki and K. Katoh, J. Magn. Magn. Mater. **54-57**, 1097 (1986).
 - ³⁶ K. Motizuki, J. Magn. Magn. Mater. **70**, 1 (1987).
 - ³⁷ R. Podloucky, J. Magn. Magn. Mater. **43**, 204 (1984).

- ³⁸ R. Podlucky, *J. Phys. F: Met. Phys.* **14**, L145 (1984).
- ³⁹ S. Sanvito and N. A. Hill, *Phys. Rev. B* **62**, 15553 (2000).
- ⁴⁰ P. Ravindran, A. Delin, P. James, B. Johansson, J. M. Wills, R. Ahuja, and O. Eriksson, *Phys. Rev. B* **59**, 15680 (1999).
- ⁴¹ A. Continenza, S. Picozzi, W. T. Geng, and A. J. Freeman, *Phys. Rev. B* **64**, 085204 (2001).
- ⁴² Y.-J. Zhao, W. T. Geng, A. J. Freeman, and B. Delley, *Phys. Rev. B* **65**, 113202 (2002).
- ⁴³ R. de Paiva, J. L. A. Alves, R. A. Nogueira, J. R. Leite, and L. M. R. Scolfaro, *Braz. J. Phys.* **34**, 568 (2004).
- ⁴⁴ A. Debernardi, M. Peressi, and A. Baldereschi, *Comput. Mater. Sci.* **27**, 175 (2003).
- ⁴⁵ A. Debernardi, M. Peressi, and A. Baldereschi, *Mater. Sci. Eng. C* **23**, 1059 (2003).
- ⁴⁶ M. Shirai and Y. Tokioka, *J. Electron Spectrosc. Relat. Phenom.* **88-91**, 357 (1998).
- ⁴⁷ K. Motizuki, K. Katoh, and A. Yanase, *J. Phys. C: Sol. Stat. Phys.* **19**, 495 (1986).
- ⁴⁸ M. K. Niranjana, B. R. Sahu, and L. Kleinman, *Phys. Rev. B* **70**, 180406(R) (2004).
- ⁴⁹ V. I. Valkov and A. V. Golovchan, *Low Temp. Phys.* **31**, 528 (2005).
- ⁵⁰ J. M. Soler, E. Artacho, J. D. Gale, A. Garcia, J. Junquera, P. Ordejon, and D. Sanchez-Portal, *J. Phys.: Condens. Matter* **14**, 2745 (2002).
- ⁵¹ J. P. Perdew, K. Burke, and M. Ernzerhof, *Phys. Rev. Lett.* **77**, 3865 (1996).
- ⁵² T. Asada and K. Terakura, *Phys. Rev. B* **47**, R15992 (1993).
- ⁵³ R. S. Mulliken, *J. Chem. Phys.* **23**, 1833 (1955).
- ⁵⁴ M. Pajda, J. Kudrnovsky, I. Turek, V. Drchal, and P. Bruno, *Phys. Rev. B* **64**, 174402 (2001).
- ⁵⁵ C. Guillaud, *J. phys. radium* **12**, 223 (1951).
- ⁵⁶ Z. S. Basinski, R. O. Kornelsen, and W. B. Pearson, *Trans. Ind. Inst. Met.* **13**, 143 (1960).
- ⁵⁷ K. Selte, A. Kjekshus, and A. F. Andresen, *Acta Chem. Scand.* **A28**, 61 (1974).